CO2 Splitting via Two-Step Solar Thermochemical Cycles with Zn/ZnO and FeO/Fe3O4 Redox Reactions: Thermodynamic Analysis

4 AUTHORS, INCLUDING:

Maria Elena Galvez
Pierre and Marie Curie University - Paris 6
66 PUBLICATIONS **828** CITATIONS

SEE PROFILE

Peter G. Loutzenhiser
33 PUBLICATIONS **581** CITATIONS

SEE PROFILE

Illias Hischier
University of Colorado Boulder
12 PUBLICATIONS **211** CITATIONS

SEE PROFILE

CO₂ Splitting via Two-Step Solar Thermochemical Cycles with Zn/ZnO and FeO/Fe₃O₄ Redox Reactions II: Kinetic Analysis

P. G. Loutzenhiser,[†] M. E. Gálvez,[‡] I. Hischier,[‡] A. Stamatiou,[†] A. Frei,[†] and
A. Steinfeld*,[†,‡]

*Solar Technology Laboratory, Paul Scherrer Institute, 5232 Villigen PSI, Switzerland, and Department of
Mechanical and Process Engineering, ETH Zurich, 8092 Zurich, Switzerland*

Two-step thermochemical cycles for splitting CO_2 with Zn/ZnO and FeO/Fe₃O₄ redox pairs using concentrated solar energy are considered. Thermogravimetric-based kinetic analyses were performed for the reduction of CO_2 to CO with Zn and FeO. Both reactions are characterized by an initial fast interface-controlled regime followed by a slow diffusion-controlled regime, which are described using a shell−core kinetic model. In the interface-controlled regime, a power rate law is applied with apparent activation energies 113.7 and 73.4 kJ mol⁻¹, and corresponding reaction orders 0.339 and 0.792, for the Zn/CO₂ and FeO/CO₂ systems, respectively. In the diffusion-controlled regime, limited by the ion mobility through the oxide shells, the apparent activation energies are 162.3 kJ mol⁻¹ for Zn/CO₂ and 106.4 kJ mol⁻¹ for FeO/CO₂. Additional reaction mechanisms above the Zn melting point for Zn/CO₂ reactions are postulated.

1. Introduction

In a previous work,[1] thermodynamic analyses were performed for two-step thermochemical cycles based on the Zn/ZnO and FeO/Fe₃O₄ redox reactions that chemically reduce CO_2 to CO or C(s) using concentrated solar energy. The first step of the cycle is the solar-driven endothermic reduction of the metal oxide, represented by:

$$ZnO \rightarrow Zn + 0.5O_2 \quad \Delta H_{298K}° = 350 \text{ kJ mol}^{-1} \quad (1)$$

or

$$Fe_3O_4 \rightarrow 3FeO + 0.5O_2 \quad \Delta H_{298K}° = 317 \text{ kJ mol}^{-1} \quad (2)$$

The second step of the cycle is the nonsolar exothermic oxidation of the metal or lower-valence metal oxide with CO_2, represented by:

$$Zn + CO_2 \rightarrow ZnO + CO \quad \Delta H_{298K}° = -68 \text{ kJ mol}^{-1} \quad (3)$$

or

$$3FeO + CO_2 \rightarrow Fe_3O_4 + CO \quad \Delta H_{298K}° = -34 \text{ kJ mol}^{-1} \quad (4)$$

A second-law (exergy) analysis for the net reaction CO_2 = CO + 0.5O₂ indicates maximum solar-to-chemical energy conversion efficiencies of 39 and 29% for the Zn/ZnO and FeO/Fe₃O₄ cycles, respectively.[1] Previous investigations dealt with the thermodynamics and kinetics of the thermal dissociations of ZnO[2−4] (eq 1) and Fe₃O₄[5,6] (eq 2). Both reactions proceeded

at reasonable rates at above about 2000 K. Recently, the solar reactor technology for ZnO dissociation was experimentally demonstrated using a 10 kW solar receiver−reactor prototype.[4] Stoichiometric and nonstoichiometric forms of wuestite ($Fe_{1-y}O$) were produced from Fe₂O₃ under an inert gas flow, with Fe₃O₄ being an important intermediary.[7] As for the second step of the cycle, most of the previous experimental studies dealt with the kinetics of Zn vapor reoxidation within the imperial smelting process.[8−11] Activation energies of ∼170 kJ mol⁻¹ were obtained for 1073−1173 K.[9] Although kinetically hindered, some traces of carbon formation were observed.[10,11] CO_2 reduction was experimentally demonstrated in exploratory studies with FeO,[12,13] oxygen-defective iron oxides,[14−17] nanocrystalline Fe₂O₃,[18] and Ni-, Co-, and Cu-doped ferrites.[19−24] Kinetic

---

* To whom correspondence should be addressed. E-mail: aldo.steinfeld@
eth.ch.
† Paul Scherrer Institute.
‡ ETH Zurich.

(1) Gálvez, M. E.; Loutzenhiser, P. G.; Hischier, I.; Steinfeld, A. *Energy Fuels* **2008,** *22,* 3544–3550.
(2) Palumbo, R.; Lede, J.; Boutin, O.; Elorza-Riccart, E.; Steinfeld, A.; Moeller, S.; Weidenkaff, A.; Fletcher, E. A.; Bielicki, J. *Chem. Eng. Sci.* **1998,** *53,* 2503–2518.
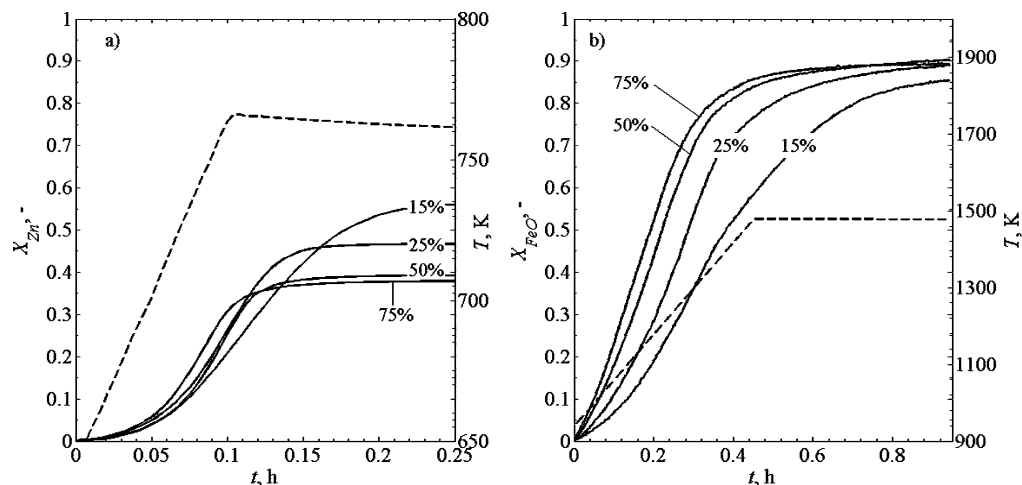(3) Steinfeld, A. *Int. J. Hydrogen Energy* **2002,** *27,* 611–619.

(4) Schunk, L. O.; Haeberling, P.; Wepf, S.; Wuillemin, D.; Meier, A.; Steinfeld, A. *J. Sol. Energy Eng.* **2008,** *130,* 021009.
(5) Tofighi A. Ph.D. Thesis, L'Institut National Polytechnique, Toulouse, France, 1982.
(6) Steinfeld, A.; Sanders, S.; Palumbo, R. *Sol. Energy* **1999,** *65,* 43–53.
(7) Charvin, P.; Abanades, S.; Flamant, G.; Lemort, F. *Energy* **2007,** *32,* 1124–1133.
(8) Clarke, J. A.; Fray, D. J. *J. Mater. Sci.* **1978,** *13,* 1921–1925.
(9) Lewis, L. A.; Cameron, A. M. *Metall. Mater. Trans. B* **1995,** *26,* 911–918.
(10) Cox, A.; Fray, D. J. *Trans. Inst. Min. Metall., Sect. C* **2000,** *109,* C97−C104.
(11) Cox, A.; Fray, D. J. *Trans. Inst. Min. Metall., Sect. C* **2000,** *109,* C105−C111.
(12) Ehrensberger, K.; Palumbo, R.; Larson, C.; Steinfeld, A. *Ind. Eng. Chem. Res.* **1997,** *36,* 645–648.
(13) Yamasue, E.; Yamaguchi, H.; Nakaoku, H.; Okumura, H.; Ischihara, K. N. *J. Mater. Sci.* **2007,** *42,* 5196–5202.
(14) Tamaura, Y.; Tabata, M. *Nature (London)* **1990,** *346,* 255–256.
(15) Zhang, C. L.; Li, S.; Wu, T. H.; Peng, S. Y. *Mater. Chem. Phys.* **1999,** *58,* 139–145.
(16) Zhang, C. L.; Li, S.; Wang, L. J.; Wu, T. H.; Peng, S. Y. *Mater. Chem. Phys.* **2000,** *62,* 44–51.
(17) Zhang, C. L.; Liu, Z. Q.; Wu, T. H.; Yang, H. M.; Jiang, Y. Z.; Peng, S. Y. *Mater. Chem. Phys.* **1996,** *44,* 194–198.
(18) Khedr, M. H.; Bahgat, M.; Nasr, M. I.; Sedeek, E. K. *Colloids Surf., A* **2007,** *302,* 517–524.

Figure 1. Reaction extent as a function of temperature and time during the dynamic TG runs with 15, 25, 50, and 75% CO_2–Ar for reactions (a) $Zn + CO_2$ and (b) $3FeO + CO_2$.
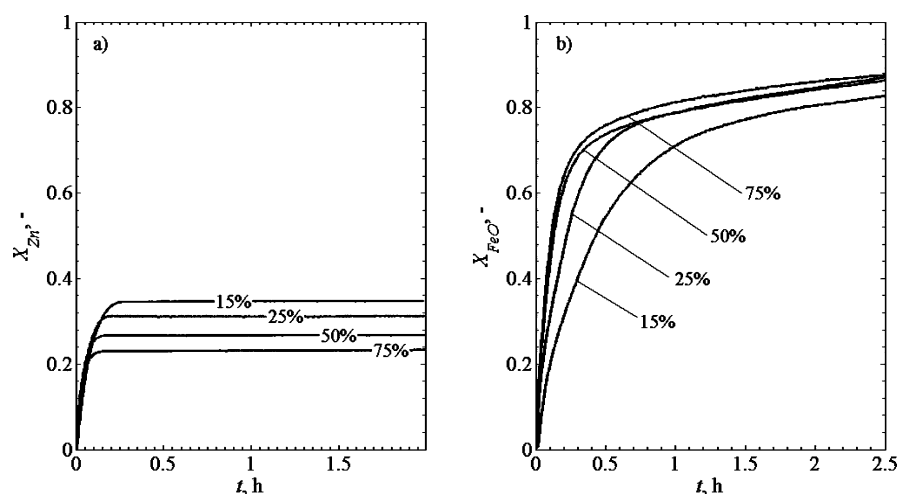

Figure 2. Reaction extents as a function of time during the isothermal TG runs with 15, 25, 50, and 75% CO_2–Ar for reactions (a) $Zn + CO_2$ at 723 K and (b) $3FeO + CO_2$ at 1173 K.

parameters for FeO and CO_2 to $FeCO_3$ in the 196–330 K range[25] and to FeO_2 in the 1330–2650 K range at atmospheric pressure[26] were also determined. Other studies extracted the rate constants using Fe[26] as a reducing agent and $MgO + CO_2$ to $MgCO_3$.[27]

The next step required to ascertain the feasibility of the proposed thermochemical cycles is to quantify the chemical reaction kinetics of the second step of the cycle, eq 3 or eq 4, which is needed for the reactor engineering design. Although thermodynamically favorable at lower temperatures, C(s) formation was never observed in this study and, therefore, is omitted from consideration. Both dynamic and isothermal thermogravimetric analyses are used to investigate the impact of the temperature and CO_2 concentration on the reaction kinetics.
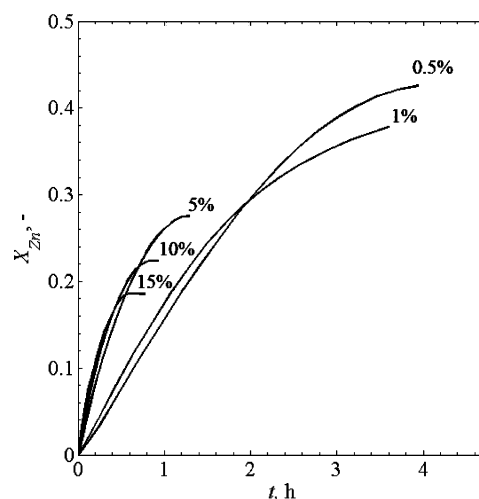
(19) Khedr, M. H.; Farghali, A. A. *Appl. Catal., B* **2005**, *61*, 219–226.
(20) Farghali, A. A.; Khedr, M. H.; Abdelkhalek, A. *J. Mater. Process. Technol.* **2007**, *181*, 81–87.
(21) Kato, H.; Kodama, M.; Tsuji, M.; Tamaura, Y. *J. Mater. Sci.* **1994**, *29*, 5689–5692.
(22) Ma, L. Y.; Chen, L. S.; Chen, S. Y. *J. Phys. Chem. Solids* **2007**, *68*, 1330–1335.
(23) Ma, L. Y.; Chen, L. S.; Chen, S. Y. *Mater. Chem. Phys.* **2007**, *105*, 122–126.
(24) Siegel, N. P. *Proceedings of the 2007 Annual AIChE Meeting*, Salt Lake City, UT, November 3–9, 2007.
(25) Rollason, R. J.; Plane, J. M. C. *Phys. Chem. Chem. Phys.* **2000**, *2*, 2335–2343.
(26) Geisen, A.; Herzler, J.; Roth, P. *Phys. Chem. Chem. Phys.* **2002**, *4*, 3665–3668.

Figure 3. Reaction extents as a function of time during the TG isothermal runs at 673 K and with 0.5, 1, 5, 10, and 15% CO_2–Ar for $Zn + CO_2$ reaction.

Appropriate rate laws are applied, and the Arrhenius rate constants are determined.

2. Experimental Section

Experimentation was carried out in a thermogravimeter system (TG, Netzsch STA 409 CD with sensitivities of ±5 μg) equipped
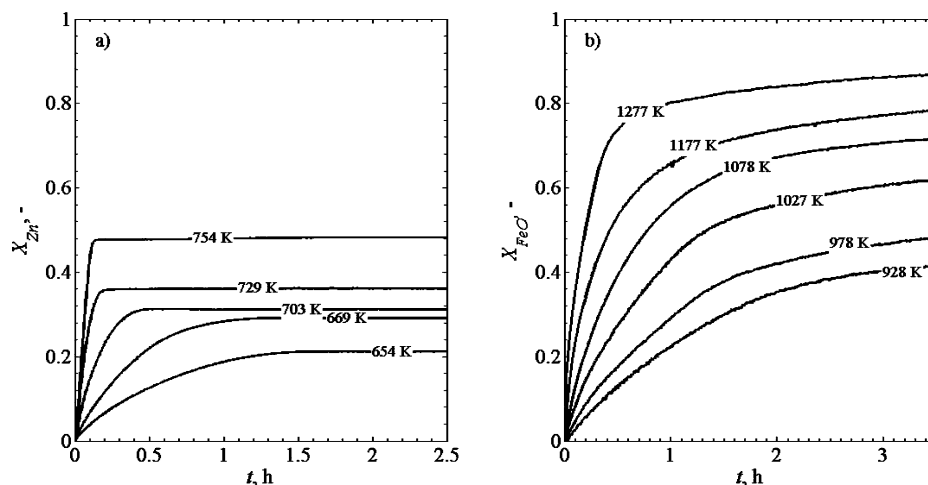
Figure 4. Reaction extents as a function of time during the isothermal TG runs with 20% CO_2–Ar at different temperatures for reactions (a) $Zn + CO_2$ and (b) $3FeO + CO_2$.
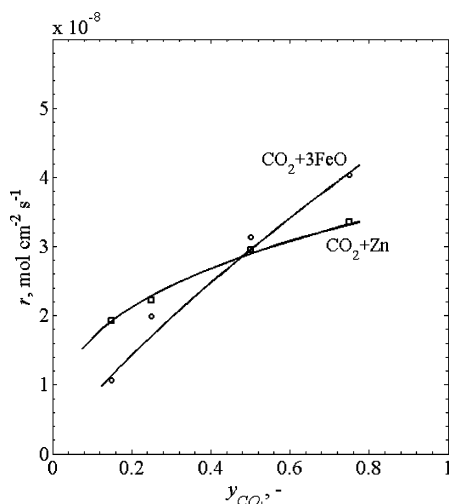

Figure 5. Reaction rates (data points) and resulting power law fits (solid lines) as function of the CO_2 molar fraction for reactions $Zn + CO_2$ at 723 K and $3FeO + CO_2$ at 1173 K in the interface-controlled regimes.

with a SiC furnace. Samples of approximately 100 mg of Zn (Sigma-Aldrich, 98+% purity, Sauter mean particle size = 11.4 μm) and FeO (Sigma-Aldrich, 99.9% pure, Sauter mean particle size = 46.4 μm) were placed on a 17-mm-diameter Al_2O_3 crucible in contact with an S-type thermocouple. Samples were first heated in Ar at a rate of 20 K/min to the desired starting temperature. Temperature was then kept constant upon the introduction of CO_2–Ar mixtures for the isothermal runs or further increased at a rate of 20 K/min for the dynamic runs. The ranges of temperature studied were 640–754 K and 923–1473 K for the $Zn + CO_2$ and the $3FeO + CO_2$ reactions, respectively. The reactant gas was fed from the bottom of the furnace and diluted with Ar for combined flows of 100 mL_N/min at various CO_2/Ar ratios (L_N denotes liters at normal conditions; mass flow rates are calculated at 273 K and 1 bar). The gas mixture flowed upward through the crucible and exited at the top. Blank runs were performed to correct for the combined effects of buoyancy and momentum on the crucible as a function of temperature. Gas flows were controlled by electronic mass flow controllers (Vögtlin QFLOW). The composition of the off-gas was monitored by gas chromatography (2-channel Varian Micro GC, equipped with a Molsieve-5A and a Poraplot-U columns) at 0.33 min^{-1} sampling rate and 100 ppm detection limit. The solid samples were characterized using their particle size distribution determined by laser scattering (HORIBA LA-950 analyzer), and surface area and porosity were characterized using Brunauer–

Emmett–Teller (BET) gas absorption method[28] with N_2 at 77 K (Micromeritics TriStar 3000). The compositions of solid samples were determined using X-ray powder diffraction (XRD, Philipps XPert-MPD powder difractometer Fe Kα, $\lambda = 1.93740$ Å, $2\theta = 20–80°$, 0.05° step) and X-ray photoelectron spectroscopy (XPS, Escalab 220i XL). The surface morphologies of the particles were examined using scanning electron microscope (SEM) images (SmartSEM, Carl Zeiss Supra 55VP). Reaction extents were calculated from the TG curves taking ZnO and Fe_3O_4 as the final solid products of the reactions $Zn + CO_2$ and $3FeO + CO_2$, respectively. No elemental carbon formation was observed, as corroborated by XRD, XPS, and mass balances. For the $3FeO + CO_2$ system, XRD analysis of the products also corroborated that the alumina crucible remained inert as no evidence of Al–Fe spinel was detected.

3. Kinetic Analysis

The mechanisms governing the oxidation of metals with O_2, H_2O, and CO_2 have been previously investigated[19,20] and comprise several stages, including physisorption and chemisorption of the oxidizing gas, formation of oxide nuclei on the surface, and diffusion of the species across this surface. The rate of these stages depends strongly on the microstructural morphology of the formed oxide layer. For Zn and FeO oxidation, two main regimes are identified: (1) an initial interface-controlled regime that proceeds relatively fast following a logarithmic,[29] linear, or parabolic[30] rate law and (2) diffusion-controlled regime that proceeds significantly slower and usually follows a parabolic rate law.[31]

The shell–core model,[32] based on the formation of a uniform oxide layer around homogeneous and spherical particles, was used in the present work to define the gas–solid reaction rates. Power and parabolic rate laws were applied to the interface-controlled (fast reaction) and the diffusion-controlled regimes (slow reaction), respectively. The data were fit to high-order polynomials for computing the analytical derivatives used to

(27) Rollason, R. J.; Plane, J. M. C. *Phys. Chem. Chem. Phys.* **2001**, *3*, 4733–4740.

(28) Sing, K. S. W.; Everett, D. H.; Haul, R. A. W.; Moscou, L.; Pierotti, R. A.; Rouquerol, J.; Siemieniewska, T. *Pure Appl. Chem.* **1985**, *57*, 603–619.

(29) Vernon, W. H. J.; Akeroyd, E. I.; Stroud, E. G. *J. Inst. Met.* **1939**, *65*, 301–329.

(30) Moore, W. J.; Lee, J. K. *Trans. Faraday Soc.* **1951**, *47*, 501–508.

(31) Szekely, J.; Themelis, N. J. *Rate Phenomena in Process Metallurgy*; Wiley: New York, 1971.

(32) Levenspiel, O. *Chemical Reaction Engineering*, 3rd ed.; Wiley: New York, 1999.

Table 1. Fitted Kinetic Parameters and 95% Confidence Limits for Power Rate Law (Eq 6) in the Interface-Controlled Regime

			reaction	
		fitted parameter	$Zn + CO_2$	$3FeO + CO_2$
isothermal TG runs	fixed T	α, $-$	0.339 ± 0.034	0.792 ± 0.100
		R^2	0.994	0.976
	fixed y_{CO_2}	$E_{a,S}$, kJ mol^{-1}	113.6 ± 1.9	73.4 ± 8.5
		$k_{0,S}$, mol s^{-1} cm^{-2}	3.61 ± 1.09	$7.68 \times 10^{-5} \pm 6.40 \times 10^{-5}$
		R^2	1	0.989
dynamic TG runs		α	0.315 ± 0.034	0.794 ± 0.028
		$E_{a,S}$, kJ mol^{-1}	113.7 ± 0.7	69.0 ± 0.0
		$k_{0,S}$, mol s^{-1} cm^{-2}	5.33 ± 0.21	$7.41 \times 10^{-5} \pm 1.14 \times 10^{-6}$
		R^2	0.988	0.973

identify the transition points from the interface-controlled to the diffusion-controlled regimes. For the dynamic experimental runs, first-order derivates were computed to estimate the reaction rates at each temperature, using a five-point symmetric finite-difference representation.[33] The data were also examined for time-series correlations and found to be independent. Nonlinear weighted least sums of squares were used to determine the parameters of the rate laws. The uncertainties from regression and propagating error analyses were used to determine weighting factors. The fits were performed in Matlab[34] using the *fminsearch* function, a multidimensional unconstrained nonlinear minimization (Nelder−Mead). The functions were formulated as:

$$f_{min}(r) = \sum_{i=1}^{n} \frac{(r_i - \hat{r}_i)^2}{\text{Var}(r_i) + \left(\frac{\partial r}{\partial T}\right)^2 \text{Var}(T_i)} \quad (5)$$

and adjusted according to the respective rate laws.

Interface-Controlled Regime. This regime is the initial fast reaction dominated by surface interactions. Three steps[35] are assumed, namely: (1) CO_2 adsoprtion on the surface, oxide nuclei formation, and desorption of CO, (2) lateral growth of oxide nuclei and formation of an oxide layer, and (3) uniform oxide layer growth. The interface-controlled regime was modeled using the following power rate law coupled with an Arrhenius-type dependency on temperature:

$$r = \frac{d}{dt}\left(\frac{n}{S}\right) = \left(\frac{p_{CO_2}}{p_{atm}}\right)^{\alpha} k_S = y_{CO_2}{}^{\alpha} k_S = y_{CO_2}{}^{\alpha} k_{0,S} \exp\left(-\frac{E_{a,S}}{RT}\right) \quad (6)$$

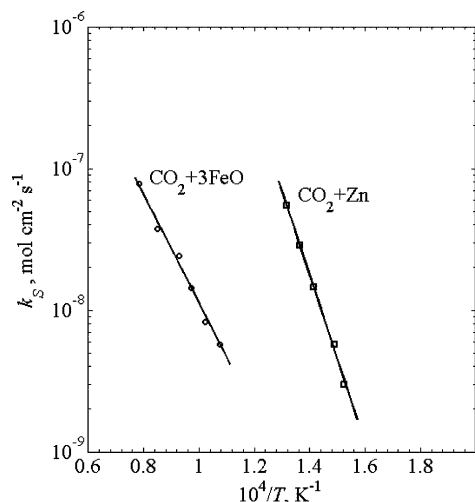where CO_2 mole fraction in the reactant gas y_{CO_2} was varied by

Figure 6. Arrhenius plots in the interface-controlled regime based on the isothermal TG runs of reactions $Zn + CO_2$ and $3FeO + CO_2$ with 20% CO_2−Ar. The power rate law (eq 6) was applied.

argon dilution at atmospheric pressure, n denotes the number of oxide moles (ZnO or Fe₃O₄), S is the surface area at the interface, p is the pressure, α is the apparent order of reaction with respect to CO_2, and k_S is the reaction rate constant with $k_{0,S}$ and $E_{a,S}$ being the apparent frequency factor and activation energy, respectively. A combination of isothermal and dynamic TG runs was used to determine α, $k_{0,S}$, and $E_{a,S}$.

Diffusion-Controlled Regime. This regime is limited by ionic diffusion and occurs at a much slower rate than the interface-controlled regime. Zn or Fe cations and O anions migrate through the oxide lattice in opposite directions, while electrons move independently from the interface to the particle surface.[36,37] Vacancies are continually created and consumed at the interface and near the surface. Ion diffusion through the oxide lattice is related to the parabolic rate coefficient. The growth rate is determined by the diffusion rate and the concentration gradients, which leads to a parabolic rate law based on Wagner's oxidation theory.[38] This parabolic rate law, coupled with an Arrhenius-type dependency on temperature, is formulated as:

$$r = \frac{d}{dt}\left(\frac{n}{S}\right) = \frac{k_P}{2(n/S)} = \frac{\rho^2 k_D}{2(n/S)M_{MO}M_O} = \frac{\rho^2 k_{0,D} \exp\left(-\frac{E_{a,D}}{RT}\right)}{2M_{MO}M_O(n/S)} \quad (7)$$

where ρ is the density of the metal oxide, k_P and the derived k_D denote the parabolic and diffusion rate constants, respectively, with $k_{0,D}$ and $E_{a,D}$ as the apparent frequency factor and activation energy, and M_{MO} and M_O are the molecular weights of the metal oxide and atomic oxygen, respectively. The reaction rate under diffusion-controlled governed by ion mobility, eq 7, was assumed to be independent of the CO_2 concentration in the gas phase. Isothermal TG runs were used to determine $k_{0,D}$ and $E_{a,D}$.

Confidence Intervals. The regression mean square errors were used with the partial derivative to estimate the confidence intervals for estimated model parameters at 95% significance levels. The confidence intervals were estimated for error propagation and parameter estimates using constant χ-squared boundaries[39] and covariance matrices,[40] while overall uncertain-

(33) Tannehill, J. C.; Anderson, D. A.; Pletcher, R. H. *Computational Fluid Mechanics and Heat Transfer*, 2nd ed.; Taylor & Francis: Washington, DC, 1997.
(34) Matlab, version 7.4.0.287 (R2007); The MathWorks: Natick, MA, 2007.
(35) Lawless, K. R. *Rep. Prog. Phys.* **1974**, *37*, 231–316.
(36) Kofstad P. *High-Temperature Oxidation of Metals*; Wiley: New York, 1966.
(37) Wagner, C. Atom Movements; National Metal Congress and Exposition, Chicago, Oct 21−27, 1950; American Society for Metals: Cleveland, OH, 1951; pp 153−173.
(38) Wagner, C. *Z. Phys. Chem. B* **1933**, *21*, 25–41.
(39) Press, W. H.; Teukolsky, S. A.; Vetterling, V. T.; Flannery, B. P. *Numerical Recipes in Fortran 77: The Art of Scientific Computing*, 2nd ed.; Cambridge University Press: New York, 1992.
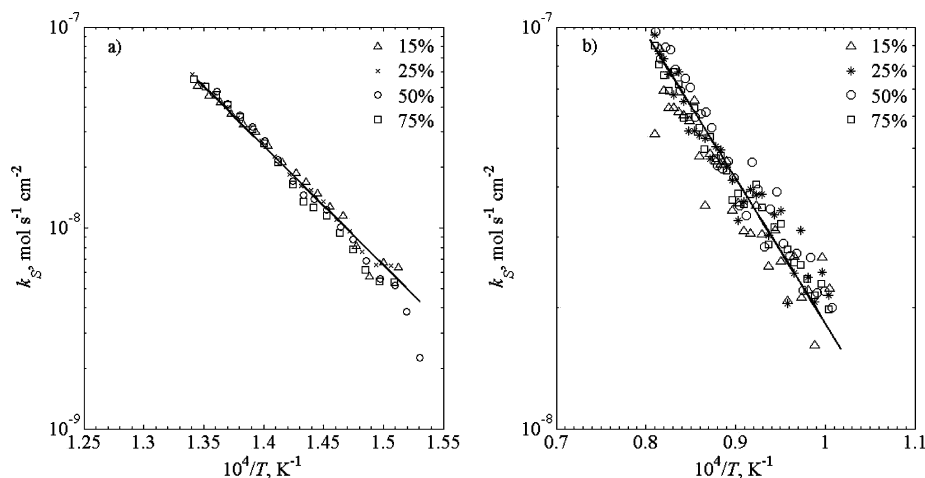
Figure 7. Arrhenius plots in the interface-controlled regime based on the dynamic TG runs of reactions (a) $Zn + CO_2$ and (b) $3FeO + CO_2$. The power rate law (eq 6) was applied.
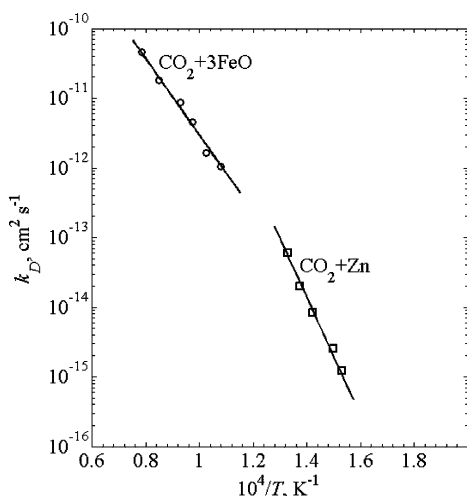

Figure 8. Arrhenius plots in the diffusion-controlled regime based on the isothermal TG runs of reactions $Zn + CO_2$ and $3FeO + CO_2$ with 20% CO_2-Ar. The parabolic rate law (eq 7) was applied.

Table 2. Fitted Kinetic Parameters and 95% Confidence Limits for Parabolic Rate Law (Eq 7) in the Diffusion-Controlled Regime

	reaction	
fitted parameter	$Zn + CO_2$	$3FeO + CO_2$
$E_{a,D}$, kJ mol^{-1}	162.3 ± 25.3	106.4 ± 8.8
$k_{0,D}$, cm^2 s^{-1}	$1.04 \times 10^{-2} \pm 4.26 \times 10^{-2}$	$1.46 \times 10^{-5} \pm 1.24 \times 10^{-5}$
R^2	0.993	0.997

ties were computed by summing the variances which are then Gaussian by the Central Limit Theorem.[41]

4. Results and Discussion

Figure 1a,b shows the reaction extents, X_{Zn} and X_{FeO}, as a function of time and temperature obtained in the dynamic TG runs performed at 20 K/min heating rates with 15, 25, 50, and 75% CO_2-Ar for reactions $Zn + CO_2$ (a) and $3FeO + CO_2$ (b), respectively. As expected for both reactions, the reaction rate increased with CO_2 concentration during the first dynamic step. X_{Zn} reached between 0.2 and 0.3 after heating from 640 to 754 K. It further increased to 0.55 at 15% CO_2-Ar during a subsequent isothermal phase. However, the final X_{Zn} decreased
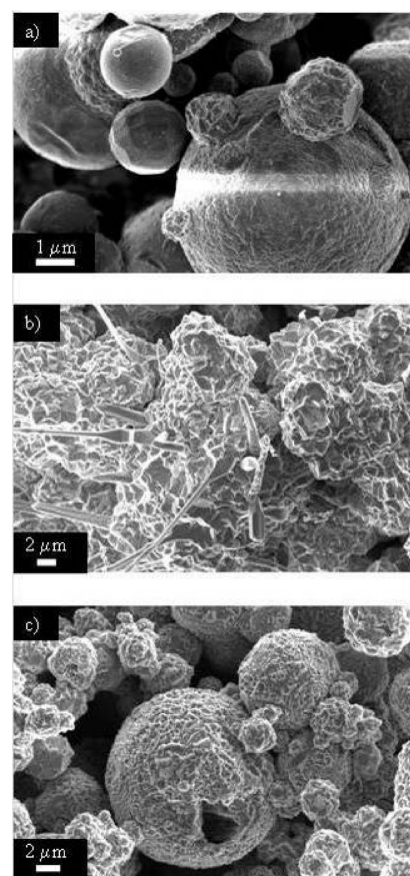
(40) Neter, J.; Kutner, M. H.; Nachtsheim, C. J.; Wasserman, W. *Applied Linear Statistical Models*; Irwin: Chicago, 1996.

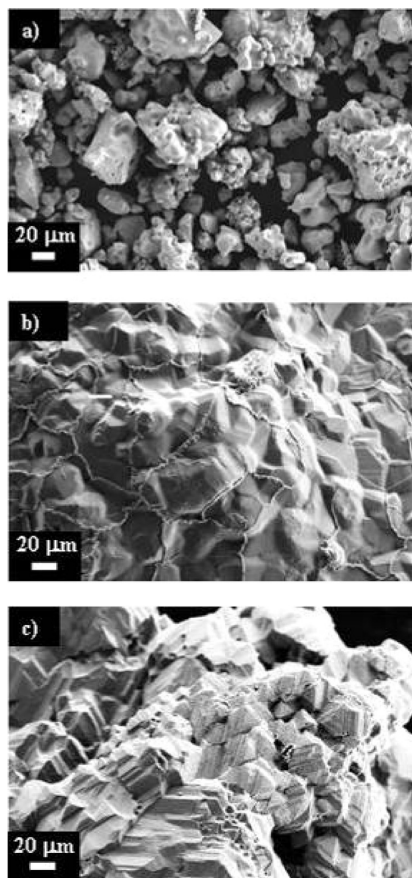(41) Gleser, L. J. *Stat. Sci.* **1998**, *13*, 277–290.

Figure 9. SEM pictures of (a) initial Zn sample, (b) product of $Zn + CO_2$ at 673 K with 0.5% CO_2-Ar, and (c) product of $Zn + CO_2$ at 673 K with 15% CO_2-Ar.

Table 3. Surface Characterization by N$_2$ Absorption of the Initial Zn Sample and the Products of $Zn + CO_2$ at 673 K with Various CO$_2$ Concentrations

reaction	S_{BET}, m^2/g	V_{micro}, cm^3/g	V_{meso}, cm^3/g
initial Zn sample	5.0	0	0.0115
1.12% CO_2-Ar	3.2	0	0.0077
5.2% CO_2-Ar	4.3	0	0.0111
10.7% CO_2-Ar	4.0	0	0.0091

as the CO_2 concentration increased, indicating a more detrimental passivation of the Zn core and faster transition to the diffusion-controlled regime. FeO oxidation in the presence of CO_2 occurred at higher temperatures than Zn oxidation. X_{FeO}

Figure 10. SEM pictures of (a) initial FeO sample, (b) product of $3FeO + CO_2$ at 978 K with 20% CO_2–Ar, and (c) product of $3FeO + CO_2$ at 1177 K with 20% CO_2–Ar.

Table 4. Surface Characterization by N_2 Absorption of the Initial FeO Sample and of the Products of $3FeO + CO_2$ with 20% CO_2–Ar at Various Temperatures

sample	S_{BET}, m²/g	V_{micro}, cm³/g	V_{meso}, cm³/g
FeO	2.1	0.0056	0.0215
20% CO_2–Ar at 928 K	4.2	0.0045	0.0111
20% CO_2–Ar at 1077 K	10.9	0.0089	0.0133
20% CO_2–Ar at 1277 K	9.4	0.0104	0.0236

ranged from 0.57 at 15% CO_2–Ar to 0.85 at 75% CO_2–Ar after heating from 923 to 1473 K. A subsequent isothermal phase resulted in a further increase of the reaction extent, with all the curves converging at $X_{FeO} \cong 0.9$, independently of the CO_2 content in the gas.

Figure 2a,b shows the reaction extents, X_{Zn} and X_{FeO}, for isothermal TG runs performed with 15, 25, 50, and 75% CO_2–Ar for reactions $Zn + CO_2$ at 723 K (a) and $3FeO + CO_2$ at 1173 K (b), respectively. In both cases, the curves exhibited initial fast interface-controlled regimes that transitioned to slow-bulk diffusion-controlled regimes, consistent with metal oxidation theory. The parabolic rate constants were computed in the diffusion-controlled regimes, which, when normalized with the active surface areas at the interface, did not significantly vary with CO_2 concentration. Thus, the primary diffusion mechanism is due to ion movements and is mainly a function of temperature. Larger X_{Zn} was observed once more at lower CO_2 concentrations, while X_{FeO} approached approximately 0.8 regardless of the CO_2 content. Regime transition occurred much faster for Zn oxidation, and reaction upon diffusion control appeared to proceed slower, as compared to FeO oxidation.

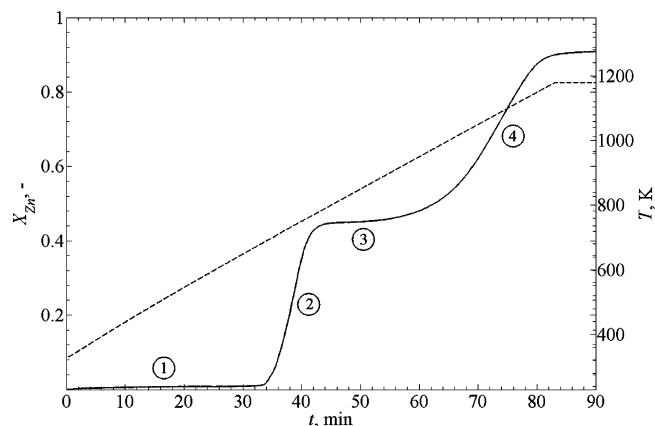Additional isothermal experiments at 673 K and with lower CO_2 concentrations in the range 0.5–15% CO_2–Ar were

Figure 11. Reaction extent (solid line) and temperature (dashed line) as a function of time for reaction $Zn + CO_2$ with 50% CO_2–Ar during a dynamic TG run.

performed for the $Zn + CO_2$ system. The results are plotted in Figure 3. The reaction rate clearly increased with increasing CO_2 content as a result of a total blockage of the Zn particles, leading to lower reaction extents at the end of the interface-controlled regime. For example, $X_{Zn} = 0.43$ at 0.5% CO_2–Ar, whereas $X_{Zn} = 0.18$ at 15% CO_2–Ar. The set of samples exposed to 1, 5, and 10% CO_2–Ar was selected for sample characterization. In the case of Zn, higher reaction temperatures, as well as higher CO_2 contents, led either to strong sample sintering or to the formation of a dense ZnO layer, which was useful in identifying the key mechanisms governing the oxidation process at lower pressures. The results garnered below 15% CO_2–Ar were not used to quantify kinetic parameters because the reaction mechanisms were different.

Figure 4a,b shows the reaction extents, X_{Zn} and X_{FeO}, for the isothermal TG runs performed with 20% CO_2–Ar at different temperatures for the reactions $Zn + CO_2$ (a) and $3FeO + CO_2$ (b), respectively. As observed in the previous figures, curves exhibited the typical shape characterized by a first fast interface-controlled regime followed by a diffusion-controlled regime. For both Zn and FeO, reaction rates as well as final reaction extents attained increased with reaction temperature, reaching $X_{Zn} = 0.5$ at 754 K and $X_{FeO} = 0.83$ at 1277 K. For the $Zn + CO_2$ reaction, the curves at 703 and 669 K approached each other, indicating a change in the reaction mechanism as Zn melts (mp 692.7 K).

Interface-Controlled Regime. Isothermal TG runs at different CO_2 concentrations were used to determine α in the integrated form of eq 6 as a function of t and n/S beginning when $t = 0$ until the transition to the diffusion-controlled regimes. The reaction rates (data points) and fitted curves (solid lines) as a function of the CO_2 molar fraction are given in Figure 5 for reactions $Zn + CO_2$ and $3FeO + CO_2$ with different CO_2 concentrations in Ar. The values of apparent order of reaction obtained, listed in Table 1, were indicative of adsorption or weak interaction between CO_2 in the gas phase and the solid surface as a previous step before reaction. The lower α for $Zn + CO_2$ pointed to stronger surface interaction as compared to that for $3FeO + CO_2$. The resulting α values were applied to the integrated form of eq 6 over the interface-controlled regime to determine the $E_{a,S}$ and $k_{0,S}$ values. Figures 6 and 7 show the corresponding Arrhenius plots for the isothermal and dynamic TG runs, respectively. Fitted parameters, 95% confidence limits, and coefficients of determination (R_2) from the dynamic and isothermal analyses are given in Table 1. $R^2 > 0.973$ for all experiments indicates good agreement with the proposed rate law for the interface-controlled regimes. Small 95% confidence
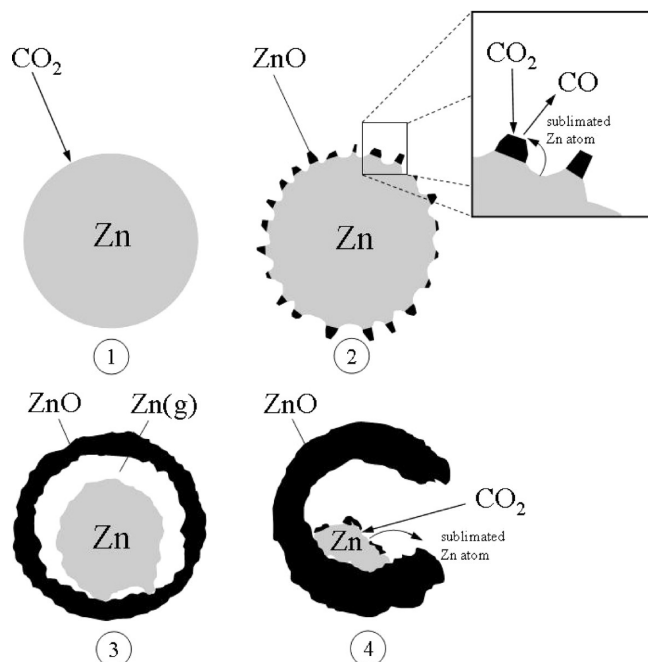
Figure 12. Schematic depicting the stages of Zn oxidation with CO_2 with increasing temperature, comprising (1) initial Zn particle exposed to CO_2, (2) interface-controlled reaction, (3) diffusion-controlled reaction of Zn^{2+} ions, and (4) development of cracks by high Zn(g) partial pressure, followed by interface-controlled reaction of Zn(g) and CO_2.
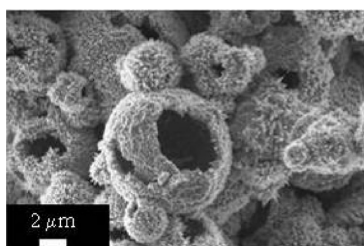

Figure 13. SEM picture of the reacted Zn/ZnO particles.

intervals for the isothermal TG runs indicate good correlations with the power rate law. The estimated parameters from the dynamic and isothermal TG runs were within 95% confidence limits and the differences are not significant, with the exception of the $k_{0,S}$ values for Zn + CO_2 which are just outside the confidence limits. The hypothesis that surface reactions are initially the dominant mechanism for the 3FeO + CO_2 reaction was verified by running a TG experiment using particles with larger surface-to-volume ratios, which resulted in faster reaction rates. For the Zn + CO_2 reaction, previous work with the Zn + H_2O reaction showed that reaction rates with Zn nanoparticles were higher than those reported with micrometer-sized particles.[42]

Diffusion-Controlled Regime. Isothermal TG runs with 20% CO_2–Ar were used to determine k_D in the integrated form of eq 7 fitting $(n/S)^2$ versus t. The initial conditions of t and $(n/S)^2$ were identified using inflection points at the transition from the interface-controlled regimes. Figure 8 shows the corresponding Arrhenius plot. Fitted parameters, 95% confidence limits, and coefficients of determination (R^2) are given in Table 2. The large uncertainties for the $k_{0,D}$ values were consistent with the experimental errors that were greater than the shallow slopes from the experiments. Higher values of $k_{0,D}$ for Zn + CO_2

together with higher values of $E_{a,D}$ pointed to lower mobility of Zn ions through the oxide layer in comparison with diffusion of Fe/O ions through the Fe_3O_4 layer. The parabolic rate law was also applied to determine the kinetics of Zn + $H_2O \rightarrow$ ZnO + H_2 for the diffusion-controlled regime, limited by zinc and oxygen ion migrations across the ZnO layer. The results at 648 K of 12.1×10^{-16} cm²/s compare well with measured results[42] at 633 K (the maximum temperature in the analysis) of $(11.9–14.45) \times 10^{-16}$ cm²/s. No similar studies for FeO were found in the literature. However, oxygen migration was presumably not the limiting step, as activation energies considerably higher than those reported here were measured for diffusion of oxygen through magnetite.[43]

Solid Characterization. XRD analyses of solid products confirmed the presence of the corresponding oxides ZnO and Fe_3O_4 and proved that the final compositions did not include carbides or other intermediate oxides. The GC measurements along with the TG mass gains confirmed that only the metal oxides and CO were produced. No evidence of C(s) formation was found. SEM images of the initial Zn sample and the reaction products (Zn/ZnO) at 673 K with 0.5% and 15% CO_2–Ar are given in Figure 9. Initial spherical Zn particles exhibited a smooth surface with sporadic irregularities caused by partial oxidation of particles exposed to ambient air. In contrast, the particle surface after reaction was generally characterized by edged uprisings of ZnO on both inner and outer shells, with directional formation of crystals noticeable in the inner shell. Most of the particles formed agglomerates. Because these experiments were conducted at the same temperatures, similar conditions with respect to the mobility of Zn ions were expected. Nevertheless, with 0.5% CO_2–Ar (Figure 9b), the particle surface exhibited fine ZnO crystal formations that grow several micrometers as long needlelike structures. The formation of such ZnO needle crystals is described in numerous studies[44–49] as a process of resublimation from the gas phase. Crystal growth in this case (needles) leads to the formation of a nonuniform oxide layer, leaving slits and interstices where CO_2 and Zn(g) can diffuse. With 15% CO_2–Ar (Figure 9c), the particles exhibited a smoother, denser ZnO layer, pointing to faster conversions under favored adsorption of CO_2, which leads to a more rapid transition to the diffusion-controlled regime consistent with observations from Figure 2a. Table 3 lists the specific surface area, micropore and mesopore volumes of the initial Zn sample, and the products of Zn + CO_2 at 673 K with various CO_2 concentrations. Relatively low values of specific surface area, absence of micropores, and small amount of mesopores (pore sizes from 1.7 to 300 nm) were observed. As these materials were practically nonporous, Zn(g) diffusion occurred presumably through interstices, defects, holes, and/or cracks in the ZnO layer.

SEM images of the initial FeO sample and the reaction products (FeO/Fe_3O_4) at 978 and 1177 K with 20% CO_2–Ar are given in Figure 10. Particles were not spherical as assumed in the kinetic model. The initial FeO particles (Figure 10a) were inhomogeneous in size and had rough surfaces. In contrast, the

(42) Ernst, F. O.; Steinfeld, A.; Pratsinis, S. E. *Int. J. Hydrogen Energy* **2009**, *34*, 1166–1175.

(43) Giletti, B. J.; Hess, K. C. *Earth Planet. Sci. Lett.* **1988**, *89*, 115–122.

(44) Cowley, J. M.; Rees, A. L. G.; Spink, J. A. *Proc. Phys. Soc., London* **1951**, *B64*, 638–644.

(45) Sears, G. W.; Powell, R.; Donn, B. *J. Chem. Phys.* **1963**, *39*, 2248–2251.

(46) Jones, K. A. *J. Cryst. Growth* **1971**, *8*, 63–68.

(47) Fujii, M.; Iwanaga, H.; Ichihara, M.; Takeuchi, S. *J. Cryst. Growth* **1992**, *128*, 1095–1098.

(48) Iwanaga, H.; Fujii, M.; Takeuchi, S. *J. Cryst. Growth* **1993**, *134*, 275–280.

(49) Muller, R.; Steinfeld, A. *Chem. Eng. Sci.* **2008**, *63*, 217–227.

product Fe_3O_4 particles had smoother surfaces. The ridges seen at lower temperatures (Figure 10b) are indicative of the lateral growth of the oxide layer after oxide nuclei formation. At higher temperatures (Figure 10c), irregularities, edged uprisings, and cracks were due to thermal stresses and faster reaction rates leading to the formation of more nuclei at the surface. There was no evidence of sublimation as in the case of Zn. Table 4 lists the specific surface area, micropore and mesopore volumes of the initial FeO sample, and the products of $3FeO+CO_2$ with 20% CO_2−Ar at various temperatures. All samples were relatively nonporous. The larger pore-specific volumes at higher temperatures were consistent with the irregularities and surface cracks observed in Figure 10c.

Zn Reaction Mechanisms. Because of the relatively low melting temperature of Zn (692.68 K) compared with that of FeO (1650 K), a dynamic TG run was performed to examine the effects of phase change during the reaction $Zn + CO_2$. Figure 11 shows the reaction extent and temperature over time during a dynamic TG run with 50% CO_2−Ar and identifies four stages indicative of different reaction mechanisms. The sample was heated from 298 to 1173 at 20 K/min. Zn oxidation began at above 690 K and proceeded almost linearly until 780 K. Concurrent formation of CO, recorded by GC, confirmed the occurrence of CO_2 reduction. After this period, the reaction proceeded at a slower rate in the 780−860 K range. Further heating to 1073 K resulted in an acceleration of the reaction that progressed to $X_{Zn} = 0.92$.

At temperatures below the Zn melting point, 693 K, ionic diffusion governed the reaction. At 823 K, the Zn evaporation rate reached 5.80×10^{-3} mol min^{-1}, enough to evaporate the entire sample in 26 min. As the temperature increased above 860 K, higher Zn(g) pressure induced surface cracks in the ZnO layer that augmented the reaction rate. The Zn(g) exiting through these cracks reacted with CO_2 on the surface of the previously formed oxide, as evidenced by the SEM picture in Figure 9c. Figure 12 depicts the various stages of the proposed reaction mechanism, comprising (1) initial Zn particle exposed to CO_2, (2) interface-controlled reaction, (3) diffusion-controlled reaction of Zn^{2+} ions, and (4) development of cracks by high Zn(g) partial pressure, followed by interface-controlled reaction of Zn(g) and CO_2. Stages 2 and 3 are consistent with the findings for solid−gas reactions presented. Further evidence of stage 4 is given in Figure 13 by the SEM picture of the product particles, revealing cracks and needlelike surfaces.

5. Summary and Conclusions

We performed a thermogravimetric analysis of the reactions $Zn + CO_2$ and $3FeO + CO_2$ as part of a two-step solar thermochemical cycle for splitting CO_2 using Zn/ZnO and FeO/Fe_3O_4 redox pairs. Two stages were identified: (1) an initial fast interface-controlled regime, described by a power rate law, and (2) a slow diffusion-controlled regime, described by a parabolic rate law. In both regimes, an Arrhenius temperature dependence of the resulting rate constants was fit to the data obtained in isothermal and dynamic TG runs.

For the $Zn + CO_2$ reaction, evaporation and surface reaction determined the progress of the reaction as the Zn(g) partial pressure inside the core increased with temperature and induced the formation of cracks and holes in the ZnO layer. Higher CO_2 concentration resulted in lower reaction extents, as the formation of a more compact and dense ZnO layer inhibited further Zn

sublimation. The kinetic parameters were extracted at 640−754 K and 15−75% CO_2−Ar from isothermal and dynamic TG runs, yielding (within 95% confidence intervals) $\alpha = 0.339 \pm 0.034$ and $E_{a,S} = 113.6 \pm 1.9$ kJ mol^{-1} for the interface-controlled regime, and $E_{a,D} = 162.3 \pm 25.3$ kJ mol^{-1} for the diffusion-controlled regime.

For the $3FeO + CO_2$ reaction, sintering and sublimation were not factors since temperatures were well below the melting point. Both temperature and CO_2 concentration influenced the reaction rate as micropore volumes and specific surface areas increased with temperature. In contrast to the reaction with Zn, the CO_2 concentration had little influence on the reaction extent with FeO. The kinetic parameters were extracted at 923−1473 K and 15−75% CO_2−Ar from isothermal and dynamic TG runs, yielding (within the 95% confidence intervals) $\alpha = 0.792 \pm 0.100$ and $E_{a,S} = 73.4 \pm 8.5$ kJ mol^{-1} for the interface-controlled regime, and $E_{a,D} = 106.4 \pm 8.8$ kJ mol^{-1} for the diffusion-controlled regime.

Comparing the two reactions, higher temperatures were required to drive $3FeO + CO_2$ with comparable reaction rates. The $Zn + CO_2$ reaction was more sensitive to changes in temperature, partly because of the lower melting point and higher partial pressure of Zn. The heat generated by the exothermal $Zn + CO_2$ reaction may have further caused punctual increase of temperature in the bulk of the sample and, consequently, local enhancement of the reaction rate. For both reactions, processes designed for quickly producing CO must avoid the diffusion-controlled regimes because of the slower kinetics. Overall, the results provide further guidance for designing reactors for splitting CO_2 and highlight the different reaction mechanisms of CO_2 with Zn or FeO.

Nomenclature

E_a = apparent activation energy
H = enthalpy
k = reaction rate constant
k_P = parabolic rate constant
k_D = diffusion rate constant
k_0 = apparent frequency factor
M_O = molecular weight of O
M_{MO} = molecular with of the metal oxide
n = moles
p = pressure
r = reaction rate
R = universal gas constant
S = surface area at the interface
S_{BET} = specific surface area from BET
t = time
T = temperature
V = specific volume
X = reaction extent
y = molar fraction
α = apparent order of reaction
ρ = density of the metal oxide

Subscripts
  atm = atmospheric
  D = diffusion-controlled regime
  i = indices
  meso = mesopore from BET
  micro = micropore from BET
  S = interface-controlled regime